

Adaptive Blind All-in-One Image Restoration

David Serrano-Lozano^{1,2} Luis Herranz³ Shaolin Su¹ Javier Vazquez-Corral^{1,2}

¹Computer Vision Center ²Universitat Autònoma de Barcelona ³Universidad Autónoma de Madrid
{dserrano, shaolin, jvazquez}@cvc.uab.cat luis.herranz@uam.es

Abstract

Blind all-in-one image restoration models aim to recover a high-quality image from an input degraded with unknown distortions. However, these models require all the possible degradation types to be defined during the training stage while showing limited generalization to unseen degradations, which limits their practical application in complex cases. In this paper, we propose a simple but effective adaptive blind all-in-one restoration (ABAIR) model, which can address multiple degradations, generalizes well to unseen degradations, and efficiently incorporate new degradations by training a small fraction of parameters. First, we train our baseline model on a large dataset of natural images with multiple synthetic degradations, augmented with a segmentation head to estimate per-pixel degradation types, resulting in a powerful backbone able to generalize to a wide range of degradations. Second, we adapt our baseline model to varying image restoration tasks using independent low-rank adapters. Third, we learn to adaptively combine adapters to versatile images via a flexible and lightweight degradation estimator. Our model is both powerful in handling specific distortions and flexible in adapting to complex tasks, it not only outperforms the state-of-the-art by a large margin on five- and three-task IR setups, but also shows improved generalization to unseen degradations and also composite distortions.

<https://aba-ir.github.io/>

1. Introduction

Image restoration (IR) is a fundamental task in computer vision, essential for enhancing visual quality and optimizing the performance of downstream tasks [37, 45]. IR aims to reconstruct high-fidelity images by systematically removing various degradations present in low-quality inputs. These degradations often emerge through a complex interplay of external environmental conditions and camera limitations during the image acquisition process such as adverse weather conditions [28, 48, 49], noise [13], blur [41] and low-light environments [4, 68].

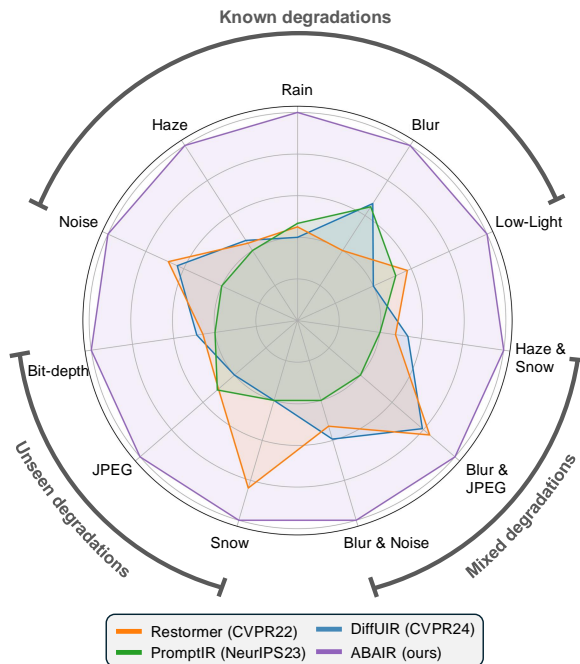


Figure 1. Our model significantly outperforms state-of-the-art all-in-one image restoration (IR) methods, Restormer [63], PromptIR [40], and DiffUIR [66], across five known IR tasks, three unseen tasks, and three mixed degradation scenarios. The plot is normalized along each axis, with the lowest value positioned on the second circle and the highest value on the outermost circle.

The inherently ill-posed nature of IR presents a significant challenge for conventional approaches limiting their effectiveness [12, 15, 18, 21, 22, 34, 38, 47]. Recent advances in deep learning techniques have led to remarkable progress in IR [11, 27, 40, 41, 63], achieving substantial improvements in reconstruction accuracy. However, these frameworks demonstrate superior performance only in modeling dedicated degradations, as they are typically trained on datasets with individual and specific IR tasks.

To address the limitations of using separate models for each degradation type, recent image restoration (IR) models have adopted an all-in-one approach, *i.e.*, they are designed to handle multiple degradation types within a single model, alleviating the dependency on dedicated models for

various IR tasks. While these models have demonstrated success in integrating diverse IR tasks into a unified framework, several challenges persist when applied to real-world IR problems. First, these models assume that the type of distortions are known in advance, allowing them to specifically target and remove them [63]. In practice, however, IR must operate in a blind setting, with no prior knowledge of the degradation present in a given image, making blind IR significantly more challenging. Second, real images frequently contain composite degradations — *e.g.*, a moving vehicle in a low-light scene, or a compressed image captured in hazy weather. Although existing models are designed to handle diverse degradation types, they typically process only a single type of distortion at a time, limiting their effectiveness in practical cases. Third, current all-in-one methods require access to all degradation types during training, which restricts their generalizability to unseen degradations. Adapting these models to new, unobserved degradation types while retaining the all-in-one functionality typically necessitates retraining the entire model with the expanded set of degradations — a process that is both computationally expensive and time-consuming.

Contribution: This paper presents an Adaptive Blind All-in-One Image Restoration (ABAIR) method, designed to bridge the gap between IR techniques and their application in practical complex scenarios. ABAIR effectively addresses multiple and composite degradations with a flexible structure that can be easily updated to include new degradations. Our approach is a simple yet effective scheme that combines three main components. First, we propose a large-scale pre-training with synthetic degradations to obtain a robust weight initialization. We propose a modified CutMix [61] to generate images under multiple distortions with a segmentation head for degradation recognition. Second, we learn disentangled restoration modules by training independent adapters — specifically LoRA [19] — to bridge the gap between synthetic and real-world data. Third, to derive a blind all-in-one IR method, we learn a lightweight image-degradation estimator to select the most suitable combination of adapters based on the input image. With the pre-training on synthetic degradations and the blending operation, our model achieves the ability to handle composite distortions within a single image. Moreover, the adapter-based design enables a flexible model structure that can be easily updated to address new distortions. We can simply train a new adapter module for the added degradation and retrain the lightweight estimator — without losing prior knowledge on other IR tasks. Our approach offers a blind all-in-one model for versatile IR, achieving superior performance on all-in-one restoration benchmarks including three- and five- degradation settings, generalizing to three unseen degradations and handling mixed degradations, as shown in Fig. 1.

2. Related Work

Single Degradation Image Restoration Most prior work on IR has typically considered removing a single type of degradation in an image to recover its clean counterpart. Typical single degradation IR tasks include denoising [13], deblurring [41], deraining [7], dehazing [59], low-light enhancement [4, 68], *etc.* Though achieving promising progress on individual tasks, these methods are only capable of dealing with a specific type of distortion, thus limiting their generalizability to a wider range of IR scenarios.

All-in-One Image Restoration Recently, multi-degradation and all-in-one IR approaches have gained significant attention. Multi-degradation methods [5, 39, 60, 62, 63] proposed unified model architectures that are effective on multiple IR tasks. However, these methods are trained in a way that one set of parameters can handle only one specific type of degradation. Therefore, one still needs to allocate different weights (though with the same architecture) for different degradations. Furthermore, to restore a versatile image, the type of degradation has to be known so that the corresponding parameters can be loaded, this non-blind scheme further hinders the efficiency and effectiveness for real-world applications.

Meanwhile, blind all-in-one IR approaches utilize specialized modules to blindly distinguish degradation types. For instance, AirNet [27] uses a contrastive-based encoder to extract a latent degradation representation from the input images. X-Restormer [8] adds a spatial self-attention module to the transformer block to enhance spatial mapping capabilities. IDR [64] learns degradation-specific priors and incorporates them into restoration, while DiffUIR [66] equips a diffusion model with a condition guidance. Despite the ability to blindly process images, these methods are still incapable of dealing with composite distortions or unseen distortions, due to their focus on dedicated degradations and standard IR benchmarks.

Prompt learning techniques, which capture task-specific context, have shown promise in guiding adaptation for vision tasks [20]. Leveraging this concept, recent methods encode degradation-specific information and guide the restoration model to enhance low-fidelity images with more than one possible distortion. PromptIR [40], for instance, integrates a dedicated prompt block to capture degradation-specific features from input images, while DA-CLIP [30], MPerceiver [2], ProRes [31] and Painter [50] leverage large pre-trained models as prompt generators. The latter approaches, however, are often constrained by high memory demands of large models. Additionally, existing all-in-one approaches require all degradation types to be predefined during training, limiting the addition of new distortion to already trained models.

In contrast, aiming at versatile image restoration, our

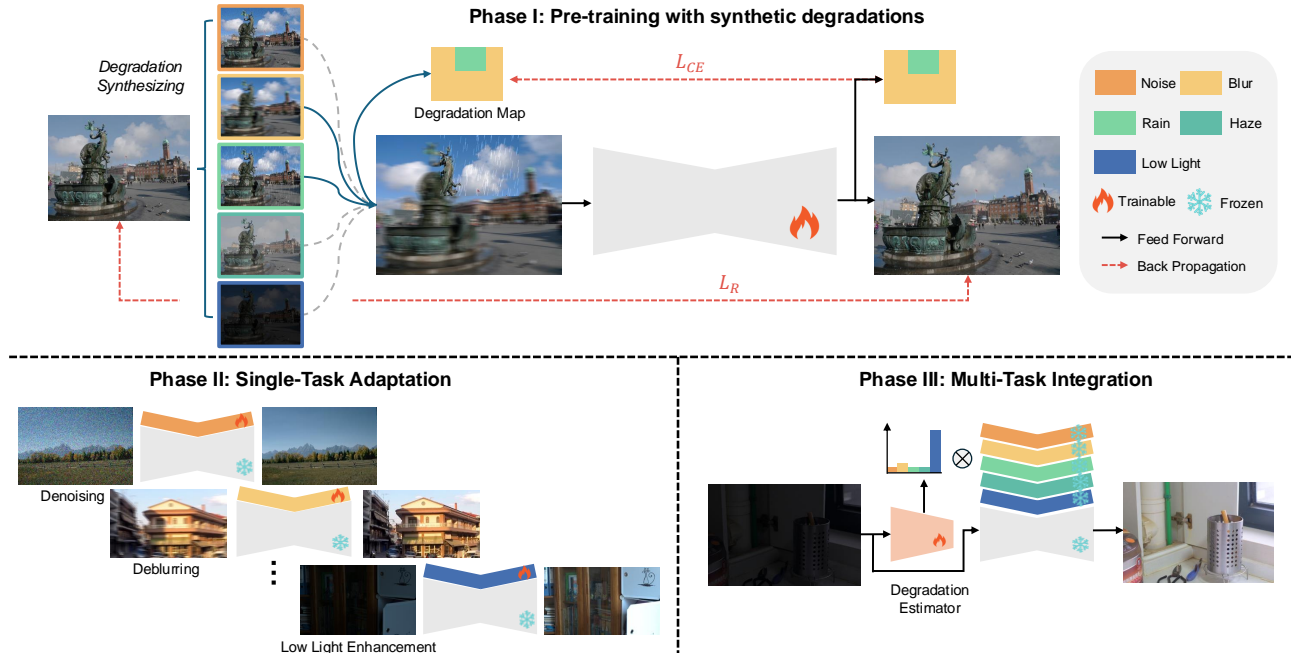


Figure 2. General schema of our proposed method. Our method is divided into three phases. In Phase I we pre-train our baseline model with synthetic degradations of high-fidelity images. Each image contains different degradations in different regions, and a segmentation head learns to predict them, while a restoration loss aims at restoring the image. In this way, the model is able to distinguish and generalize well to multiple degradations. In Phase II, we learn degradation-specific adaptors using standard image restoration datasets. In Phase III, we learn a lightweight degradation estimator to adaptively blend the adaptors based on the degradation profile of the input image. This 3-phase methodology makes our method flexible to deal with images containing multiple distortions and easy to update for new ones as it only requires training an adaptor for the new distortion and retraining the degradation estimator.

model is developed to blindly process images with various kinds of distortion, either in single or composite forms. With the mixed design of lightweight degradation adaptors, our model is also flexible and extensible to unseen distortions, thus shows great generalizability towards the challenging blind all-in-one IR problem.

Parameter Efficient Fine-Tuning Fine-tuning models by updating all parameters is computationally inefficient, especially for large-scale models. Parameter Efficient Fine-Tuning (PEFT) addresses this by reducing the number of trainable parameters and memory usage while achieving comparable performance to full fine-tuning [54]. Low-Rank Adaptation (LoRA) [19] introduced a reparametrization strategy for fine-tuned weights, where the weights of a specific layer $W' = W + \Delta W$ are represented as a linear combination of the pre-trained weights W and the updated term ΔW obtained through a low-rank decomposition, $\Delta W = BA$. Here, $B \in \mathbb{R}^{d \times k}$, $A \in \mathbb{R}^{r \times k}$ with rank $r \ll \min(d, k)$. By optimizing only the low-rank matrices A and B , LoRA reduces the number of parameters required for adapting that layer (vs tuning all parameters), minimizing memory and computational demands. Building upon LoRA, alternative decomposition methods have been proposed, such as Vector-based Random Matrix Adap-

tation [24] and Conv-LoRA[67].

PEFT techniques have proven valuable not only for domain adaptation in large models but also for applications like task arithmetic and continual learning, mitigating the problem of catastrophic forgetting—where models lose previously acquired knowledge upon learning new tasks[10]. In IR, Park et al. [39] applied low-rank decomposition within single-task IR frameworks to enhance model performance. In contrast, we propose a simple but novel approach to merge different adaptors — LoRAs — to obtain a flexible blind all-in-one model capable of learning new tasks without forgetting previously learned IR tasks. This is achieved through a disentangled scheme that requires minimal retraining for each new task.

3. Method

Figure 2 presents an overview of our proposed approach for enhancing low-quality images by systematically addressing the key limitations in current IR methods. Our approach consists of three phases, roughly targeting the following challenges: (i) robust generalization to varying types of degradations (Phase I), (ii) effective adaptation to specific degradations (Phase II), (iii) flexible all-in-one mechanism able to handle unknown and mixed degradations (Phase III).

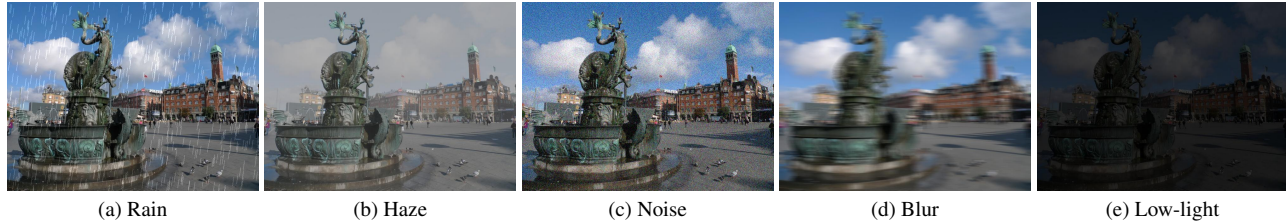


Figure 3. Examples of our synthetic degradation generation for five traditional distortions.

Note that we freeze the parameters of baseline after Phase I and adapters after and II, thus preserving maximal knowledge learned from previous tasks and avoid catastrophic forgetting. This design also allows us to adapt to new distortions with minimal additional training as only a new adapter and the light-weighted estimator will be trained.

Phase I: Pre-training with synthetic degradations. Recent advances demonstrate that large-scale pre-trained models can significantly improve performance across various tasks [1]. Moreover, pre-training with synthetic data has also shown effectiveness when the domain gap is properly addressed [55]. We hypothesize that applying large-scale pre-training to IR can yield a notable performance boost compared to training solely on traditional IR datasets. Thus, as depicted in Fig. 2, Phase I involves training a baseline IR model with large-scale data with synthetic degradations to provide a robust weight initialization for handling complex degradations.

To obtain large-scale data for pre-training, we define a degradation pipeline that generates a low-quality counterpart for each high-quality input image by introducing different synthetic distortions. We focus on five common distortions: noise, blur, rain, haze, and low-light conditions. Each synthetic distortion closely approximates its real-world counterpart. For instance, low-light conditions are simulated by compressing the image histogram, reducing the dynamic range of pixel intensities. In contrast, haze is introduced by adding an achromatic layer based on the depth map estimated from DepthAnythingv2 [55]. Figure 3 illustrates examples of each synthetic degradation. We use the Google Landmarks dataset (GLD) [53], a large-scale collection of five million images of diverse landmarks worldwide. To ensure that the inputs to our pipeline are high quality, we filter out the images with a resolution smaller than 400 pixels on any side and exclude images with a NIMA score [46] below the 4.90 threshold, retaining only high-quality natural images.

To construct our baseline model, we build on recent advancements in all-in-one IR methods. Particularly, we use the Restormer architecture [63] with spatial attention mechanisms [8] and incorporate a modified version of PromptIR [40] prompt blocks. This combination enables the baseline model to effectively capture the inherent information of various degradations, establishing a strong foundation for

generalized IR tasks.

While training on single distortions enables the model to address each type individually, real-world IR often involves mixed degradations. However, directly applying multiple distortions to an image often leads to severe quality degradation, making it difficult for the model to learn to reconstruct the original image. To tackle this, we implement two strategies: (i) a degradation CutMix [61] technique, and (ii) a segmentation head with a cross-entropy loss. Our first strategy — inspired by Yang et al. [55] for depth estimation — applies two different degradations divided into different regions. This setup helps the model distinguish and manage multiple degradation types within the same image. As our second strategy, we incorporate a segmentation head into the baseline model, which outputs a per-pixel map of the distortions. By comparing this map with the ground truth, we guide the model to recognize and differentiate multiple types of degradation within a single image. We report additional details about our baseline and the generation of the synthetic distortions in the Supplementary Material.

Phase II: Single-task adaptation. By generating distortions synthetically, we achieve a robust weight initialization for our baseline model. However, a domain gap persists between our pre-training data (due to both the different dataset and the synthetic distortions), standard IR datasets, and real-world conditions. For instance, accurately simulating haze is particularly challenging due to its dependence on light scattering by particles, which varies with depth and atmospheric conditions. To bridge this gap, we propose adapting the baseline model with adapters learned for each specific task in its standard dataset, representing Phase II of our approach, as outlined in Fig. 2.

In our approach, each linear and convolutional layer is augmented with a set of LoRA, one per type of degradation, parametrized by $\{A_n\}$ and $\{B_n\}$ where n is the index of the degradation. Following LoRA, these low-rank matrices adjust the initial frozen weights through linear combinations, as described earlier. For simplicity, we omit the subindex indicating the specific layer of the model, but each layer has a separate set of adapters. Due to the proposed pre-training approach and the subsequent specialization via adaptation, our approach achieves superior performance across diverse tasks and generalizes effectively.

Table 1. 5-degradations setup. Quantitative results on five IR datasets comparing the state-of-the-art all-in-one methods and our approach. *Ours (Oracle)* is an upper bound for our approach: it computes the best reachable value in case our estimator always chooses the correct degradation.

PSNR/SSIM	Deraining		Dehazing		Denoising		Deblurring		Low-Light		Average		Param.
	Rain100L		SOTS (Out)		BSD68 $\sigma=25$		GoPro		LoLv1				
AirNet [27]	32.98	.951	21.04	.884	30.91	.882	24.35	.781	18.18	.735	25.49	.847	9M
Uformer [51]	35.48	.967	27.20	.958	30.59	.869	26.41	.809	21.40	.808	28.21	.882	52M
IDR [64]	35.63	.965	25.24	.943	31.60	.887	27.87	.846	21.34	.826	28.34	.893	15M
X-Restormer [8]	35.42	.968	27.58	.959	30.92	.880	27.54	.835	20.88	.817	28.47	.891	26M
DA-CLIP [30]	35.49	.970	28.10	.962	30.42	.859	26.50	.807	21.94	.817	28.49	.880	174M
DiffUIR [66]	35.52	.969	28.17	.964	30.92	.879	26.99	.821	20.92	.789	28.50	.880	36M
Restormer [63]	35.56	.970	27.94	.962	30.74	.875	26.84	.818	21.74	.815	28.56	.888	26M
PromptIR [40]	35.40	.967	28.26	.965	30.89	.872	26.55	.808	21.80	.815	28.58	.885	36M
Ours OH	<u>37.73</u>	<u>.978</u>	<u>33.46</u>	<u>.983</u>	<u>31.38</u>	.898	29.00	.878	24.20	.865	<u>31.15</u>	<u>.920</u>	59M
Ours SW	37.79	.979	33.48	.984	<u>31.38</u>	.898	29.00	.878	<u>24.19</u>	.865	31.17	.921	59M
Ours (Oracle)	39.09	0.981	33.54	.984	31.40	0.901	29.10	.879	24.45	.866	31.39	.922	59M

Phase III: Multi-task integration. While LoRA adapters serve as a plug-and-play solution for pre-trained models, there is still the need to select the most suitable adapter based on the input image, when the type of degradation is unknown. To address this limitation and derive a blind all-in-one IR method, we propose to use a lightweight degradation estimator $p(n|x;\theta)$ to estimate the probability of each degradation n given the input image x , parametrized by θ . This estimator is trained on the combination of all (seen) datasets, thus learning to identify the type of degradation present in the image. As shown in Fig. 2, the probability of the estimator is used as weights to linearly combining the task-specific adapters with the baseline parameters. Specifically, given an input image x , the weight update for a specific layer with baseline weights W and adapter weights $\{A_n\}$ and $\{B_n\}$ is computed as:

$$W'(x) = W + \sum_{n=1}^N p(n|x;\theta) B_n A_n, \quad (1)$$

where N is the number of seen degradations.

We propose two variants of the estimator: (i) one-hot and (ii) soft-weights. The one-hot variant simply selects the adapter corresponding to the degradation with the maximum probability (equivalent to 1 with one-hot probabilities), while the soft-weight variant uses computes the weighted average as in Eq. (1).

Our approach allows the model to linearly combine the degradation-specific knowledge to address both specific and multiple distortions. Its modular and parameter efficient architecture also allows to add additional degradations with small training effort: train additional adapters for the new task, and update the estimator.

4. Experiments

We evaluate our method on two setups for all-in-one IR: five- and three-degradation setups. Additionally, we test on datasets excluded from training, novel IR degradation types, and mixed degradation scenarios. The accuracy of the methods is assessed using two well-established metrics: PSNR and SSIM. In all cases we report the mean value for all the test images, and we highlight **best** and **second-best** values for each metric. Our approach is compared against recent all-in-one IR methods. Notably, some current methods are either evaluated under different setups or lack available code and models, which complicates direct comparisons. Therefore, we train three state-of-the-art methods, Restormer [63], PromptIR [40], and X-Restormer [8], on the five-degradation IR setup to provide a fair comparison. We used the authors' provided code. For our approach, we evaluate the two variations based on the variants of the estimator, namely one-hot (OH) and soft weights (SW).

Implementation details: Our training is conducted in three phases using Adam [23] with weight decay [29], an initial learning rate of 2×10^{-4} , a cosine learning rate scheduler, and a warmup start of one epoch. In phase I, we apply a weighted combination of cross-entropy loss L_{CE} for per-pixel degradation maps and a reconstruction loss L_R , where L_R consists of L_1 loss and SSIM loss. Both the cross-entropy and SSIM components are weighted with 0.5. In phase II, we use only the reconstruction loss, where, as before, SSIM loss is weighted with 0.5. In phase III, we apply cross-entropy loss between the regressor's output and the input image's degradation type.

Table 2. 3-degradations setup. Quantitative results on three IR datasets comparing the state-of-the-art all-in-one methods and our approach.

PSNR/SSIM	Deraining		Dehazing		Denoising					Average		
	Rain100L		SOTS (Out)		BSD68 $\sigma=15$		BSD68 $\sigma=25$		BSD68 $\sigma=50$			
DL [14]	32.62	.931	26.92	.931	33.05	.914	30.41	.861	26.90	.740	29.98	.875
MPRNet [62]	33.57	.954	25.28	.954	33.54	.927	30.89	.880	27.56	.779	30.17	.899
AirNet [27]	34.90	.967	27.94	.962	33.92	.933	31.26	.888	28.00	.797	31.20	.909
Restormer [63]	35.56	.969	29.92	.970	33.86	.933	31.20	.888	27.90	.794	31.69	.911
PromptIR [40]	36.37	.972	30.58	.974	33.98	.933	31.31	.888	28.06	.799	32.06	.913
Ours OH	38.58	.981	33.71	.985	<u>33.95</u>	.934	31.29	.889	<u>28.04</u>	<u>.798</u>	33.11	.918
Ours SW	<u>38.52</u>	<u>.980</u>	<u>33.62</u>	<u>.984</u>	<u>33.95</u>	<u>.933</u>	31.24	.889	28.01	.796	<u>33.07</u>	<u>.916</u>

Table 3. Quantitative results on additional test datasets with the learned degradations.

PSNR/SSIM	Deraining		Deblurring		Low-Light	
	Rain100H		HIDE		LolV2-Real	
IDR [64]	11.32	.397	16.83	.621	17.61	.697
X-Restormer [8]	14.08	.437	25.40	.801	25.42	.876
DiffUIR [66]	14.78	.487	23.98	.739	26.12	.861
Restormer [63]	14.50	.464	24.42	.781	27.12	.877
PromptIR [40]	14.28	.444	24.49	.762	27.70	.870
Ours OH	21.69	.692	<u>27.04</u>	.850	28.09	.907
Ours SW	<u>19.37</u>	<u>.594</u>	27.05	.850	28.09	<u>.906</u>

Table 4. Quantitative results for unseen IR tasks. Note that the models have not been trained for these degradations. Ours* shows results for the lightweight re-training scenario. New adapters are trained for the new tasks and the estimator is retrained with 8 tasks (5-IR case + 3 new ones; only 8M training parameters).

PSNR/SSIM	4-to-8 bits		JPEG Q20		Desnowing	
	Live1		Live1		City-Snow	
IDR [64]	24.02	.738	26.51	.913	18.00	.649
X-Restormer [8]	24.73	.745	26.86	.922	18.51	.681
DiffUIR [66]	24.68	.743	26.88	.921	18.39	.671
Restormer [63]	24.64	.743	26.90	.929	18.14	.655
PromptIR [40]	24.70	.740	26.60	.920	18.49	.673
Ours OH	<u>25.25</u>	<u>.742</u>	<u>29.20</u>	<u>.931</u>	18.71	.684
Ours SW	25.32	.743	29.35	.926	<u>18.67</u>	<u>.683</u>
Ours OH*	29.14	.826	30.82	.943	24.19	.797
Ours SW*	29.03	.810	30.71	.939	24.02	.779

5-Degradation blind IR: For the blind five-task setup, we follow the protocol by Zhang et al. [64]. Specifically, we use Rain200L [56] for deraining, RESIDE [25] for dehazing, BSD400 [33] and WED [32] for denoising with $\sigma = 25$, GoPro [35] for deblurring, and LOL [52] for low-light enhancement. For evaluation, we employ Rain100L [56], SOTS-Outdoor [25], BSD68 [33], GoPro [35], and LOL [52]. Results are reported in Tab. 1. Our

approach outperforms all state-of-the-art methods across all tasks, with the exception of PSNR for denoising. Notably, our method achieves a substantial improvement over the state of the art, yielding a 2.91 dB average PSNR gain across the five tasks. In particular, our method surpasses IDR [64] by 2.16 dB on image deraining and provides a 2.40 dB improvement over PromptIR [40] on low-light image enhancement.

3-Degradation Blind IR: Following Li et al. [27], we further evaluate our approach on a 3-task blind IR setup, comparing our approach with specialized all-in-one methods for deraining, dehazing, and denoising. Compared to the five-task setup, we omit deblurring and low-light enhancement and instead introduce two additional noise levels: $\sigma = 15$ and $\sigma = 50$. Two LoRA adapters for these noise levels are trained, and the estimator is retrained for the new setting. Results for this 3-task setup are presented in Tab. 2. Our approach outperforms all the other state-of-the-art methods on average and stays consistent in all the degradation types.

Additional test sets: To assess the generalization capabilities of our approach, we evaluate the model on three datasets not used during training. Specifically, we use the Rain100H [56] dataset for heavy deraining, HIDE [43] for human-centric deblurring, and LoLv2-Real [58] for low-light image enhancement. The results of the three best methods on the 5-degradation setup and our approach are presented in Tab. 3. Our method outperforms all other approaches across all datasets and metrics. Notably, we achieve a significant improvement of 7.19 dB over Restormer [63] on Rain100H [56]. This performance boost can be attributed to the pre-training on synthetic data, which allows our model to learn from a broader set of natural images and degradation scenarios compared to the other methods’ small training set, like Rain200L [56]. Additionally, we achieve over 1 dB PSNR improvement on both HIDE and LoLv2-Real, further demonstrating the effectiveness and robustness of our approach.

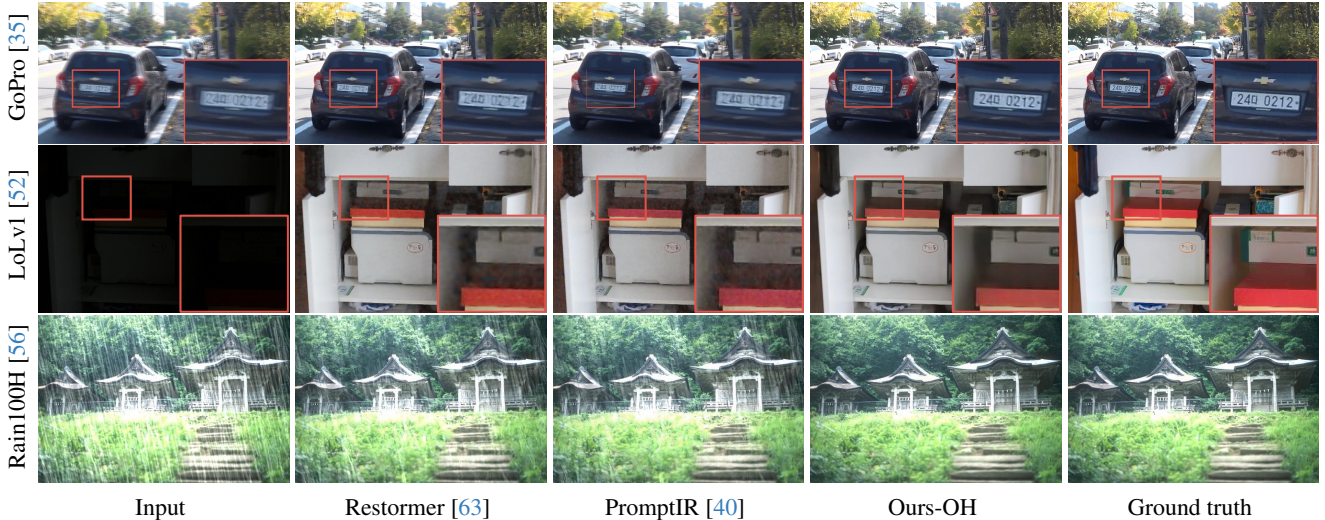


Figure 4. Qualitative results for single degradation removal, including deblurring on the GoPro [35] dataset, denoising on the LoLv1 [52] dataset, and deraining on the Rain100H [56] dataset.

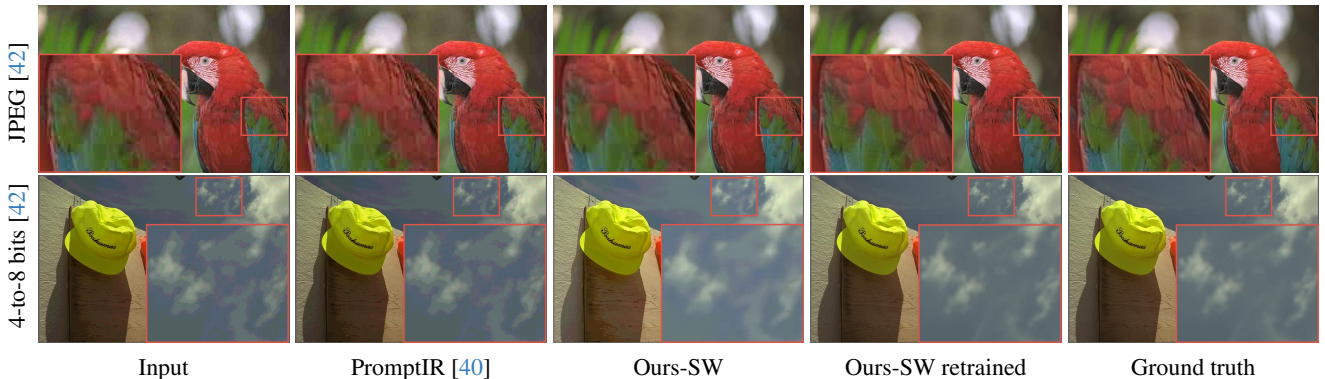


Figure 5. Qualitative results for unseen IR tasks, including JPEG artifact removal and 4-to-8 bit reconstruction. PromptIR [40] and Ours are not trained for this task, while Ours retrained has a specified LoRA in an 8-degradation setup.

Unseen IR tasks: Although our approach was initially trained on five types of degradations, we further evaluate its generalization to three additional IR tasks not encountered during training. Specifically, we assess our method on JPEG artifact removal and bit-depth reconstruction using the Live1 dataset [42], and on desnowing using CityScapes-Snow-Medium [65]. Results for the top four previous state-of-the-art methods from the five-degradation setup, alongside our approach, are presented in Tab. 4. Remarkably, our method outperforms all other approaches across all tasks and metrics. To show the adaptability of our approach, we additionally train a separate adapter for each new task, along with a new estimator that blends all eight task-specific adapters, thereby expanding the model’s versatility. The last two rows of Tab. 4 report results for the newly integrated tasks — shown with a *. Notably, with the addition of these task-specific adapters, our model achieves a notable boost in performance, while maintaining an average PSNR of 30.08 dB across the original five IR tasks, outperforming the other state-of-the-art methods trained on the initial setup.

Mixed degradations: The limited availability of datasets with mixed degradations presents a challenge for training IR models under these complex conditions. To evaluate our approach, we evaluate it on three mixed-degradation scenarios: blur combined with noise $\sigma=25$ using the Go-Pro dataset[35], blur with JPEG artifacts using the REDS dataset [36], and haze combined with snow using the SRRS dataset [6]. Notably, some degradations, such as JPEG artifacts and snow, are unseen during training, further increasing the difficulty of these tests. As shown in Tab. 5, our model consistently outperforms other methods across all scenarios and metrics. Handling blur with noise is particularly challenging due to their contrasting nature: blur affects low frequencies, while noise affects high frequencies. Even though, our model achieved around 2dB improvement while others remained at the level of 22dB.

Qualitative results: In Fig. 4, we present examples featuring three types of single degradations from the five-task setup on which the model was trained. Our approach effec-

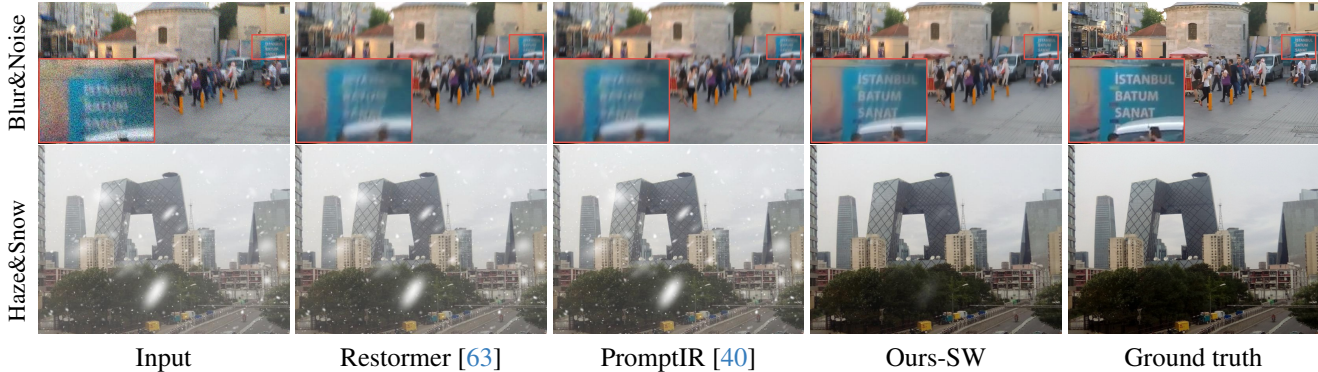


Figure 6. Qualitative results for two examples of mixed degradations. The first row depicts an image with blur and noise from the GoPRO dataset [35], while the second row shows an image with haze and snow from the SRRS dataset [6]. Columns display the input image, results from Restormer [63], PromptIR [40], our method, and the ground truth, respectively.

Table 5. Quantitative results on datasets with mixed degradations.

PSNR/SSIM	Blur&Noise		Blur&JPEG		Haze&Snow	
	GoPro		REDS		SRRS	
IDR [64]	21.98	.683	23.02	.681	20.51	.789
X-Restormer [8]	22.67	.669	23.98	.710	20.76	.805
DiffUIR [66]	22.71	.670	24.00	.711	20.86	.802
Restormer [63]	22.35	.662	23.24	.698	20.76	.800
PromptIR [40]	22.89	.671	23.92	.705	20.94	.803
X-Restormer [8]	22.67	.669	23.98	.710	20.76	.805
Ours OH	24.30	.743	24.81	.717	21.48	.834
Ours SW	25.14	.750	24.97	.719	22.09	.839

Table 6. Ablation studies on types of pre-training for Phase I, and the rank of LoRA [19] for Phase II and III.

Pre-training	PSNR	SSIM	Rank	PSNR	SSIM	Params
IR datasets	28.50	.892	4	31.17	.921	3.6M
GLD+synth.	30.63	.913	8	31.14	.920	7.2M
+ CutMix	31.09	.920	16	30.97	.916	14.3M
+ Aux. segm.	31.17	.921				

tively enhances the license plate in the first row, reduces noise in low-light conditions in the second row, and removes heavy rain streaks in the third. In Fig. 5, we show unseen IR tasks including JPEG artifact removal and 4-to-8-bit reconstruction using the Live1 dataset [42]. Our method successfully removes JPEG artifacts from the parrot’s plumage and artifacts caused by bit-depth reduction from the cloud and blue sky. By training a new adapter for these tasks (ours-SW retrained), we achieve superior results with minimal additional training time. Finally, in Fig. 6, we demonstrate our method’s performance under mixed degradations. The first row shows that our method achieves the best reconstruction of the text in the image, while the second row illustrates our model’s effectiveness in removing both haze and snowflakes.

Ablation studies: In Tab. 6, we perform an ablation study to assess the contribution to the final performance of the proposed pre-training pipeline and the LoRAs’ rank. For pre-training in Phase I, we use the same setup as the five-task configuration, *i.e.* training the LoRAs and the estimator using task-specific IR datasets and the obtained pre-trained weights. The first row — IR datasets — reflects pre-training on standard IR benchmarks, yielding performance comparable to state-of-the-art methods — see Tab. 1. In contrast, simply pre-training on GLD with synthetic degradations improves performance by 2.15 dB PSNR, demonstrating the importance of Phase I to provide the model with strong generalization capabilities. Further incorporating both the CutMix-like [61] strategy and the auxiliary segmentation task provides an additional performance boost. We also compare LoRA [19] with different ranks for Phase II and III. The model achieves the best performance and efficiency when the rank is set to 4, which we adopted as our default setting. For more ablation results, please refer to our Supplementary Material.

5. Conclusion

In this work, we introduced an adaptive blind all-in-one IR model aiming towards practical IR. We design both dedicated adapters for strongly handling specific distortions but also a flexible architecture for dealing with practical IR challenges. We first developed a pre-training pipeline featuring multiple synthetic degradations over a large dataset that boosts the generalization of the model. Second, we derived compact per-task adapters that robustly adapt to specific degradations. Third, we developed a lightweight degradation estimator that identifies varying degradations to blend the respective adapters, which is also capable of efficiently incorporate new degradations by training a small fraction of parameters. Our model largely outperforms the state-of-the-art on five- and three-task IR setups, and shows improved generalization to unseen datasets and IR tasks.

Acknowledgements

DSL, LH, and JVC were supported by Grant PID2021-128178OB-I00 funded by MCIN/AEI/10.13039/501100011033 and by ERDF "A way of making Europe", by the Departament de Recerca i Universitats from Generalitat de Catalunya with reference 2021SGR01499, and by the Generalitat de Catalunya CERCA Program. DSL also acknowledges the FPI grant from Spanish Ministry of Science and Innovation (PRE2022-101525). LH was also supported by the Ramon y Cajal grant RYC2019-027020-I. SS was supported by the HORIZON MSCA Postdoctoral Fellowships funded by the European Union (project number 101152858)

6. Supplementary Material

We provide additional material to supplement our main submission. Specifically, we cover:

- A. Details on our baseline architecture.
- B. Description of the generation process for synthetic degradations, including rain, haze, noise, blur, and low-light conditions. Additional dataset examples.
- C. Additional ablation experiments on LoRA's rank and other decomposition methods.
- D. Details on our estimator architecture and additional analysis of the estimator's performance.
- E. Additional qualitative results on known datasets, unseen tasks, and images with mixed degradations.

A. Baseline Architecture Details

We present an Adaptive Blind All-in-One Image Restoration (ABAIR) method, designed to bridge the gap between IR techniques and their application in practical complex scenarios. Our approach follows a three-phase scheme. The first phase involves pre-training an IR baseline using natural images with synthetic degradations. In this section, we describe this baseline architecture. Figure 7 shows the details of our baseline model. Our baseline model adopts the Restormer [63] architecture, a transformer-based UNet-like framework. Given a degraded image, the model first applies a convolutional layer to extract low-level features of size $H \times W \times C$, where H and W are the spatial dimensions, and $C=48$ in all our experiments. These features are then processed through a four-level encoder-decoder structure composed of transformer blocks, with pixel unshuffling and shuffling [44] used for downsampling and upsampling, respectively. Finally, a convolutional layer generates the residual image, which is added to the degraded input image to produce the restored output.

Each transformer block comprises a channel self-attention module followed by a spatial self-attention module. For channel self-attention, we adopt the implementation from Zamir et al. [63], while for spatial attention, we

use the overlapping cross-attention mechanism proposed by Chen et al. [9]. This combination effectively addresses the limitations of Restormer's U-shaped architecture, particularly its difficulty in reconstructing high-frequency details [8]. Additionally, inspired by Potlapalli et al. [40], we integrate a Prompt Block between the transformer blocks in the upsampling path. This block facilitates the architecture in identifying degradation-specific features in the input image by combining extracted features with a set of model parameters. The design of our Prompt Block is depicted in Fig. 8.

B. Synthetic Degradations Generation

The first phase of our approach involves pre-training the baseline model using natural images with synthetically generated degradations, including rain, haze, noise, blur, and low-light conditions. Unlike standard IR datasets, our pipeline introduces degradations dynamically to clean input images, offering greater flexibility by enabling the model to be trained on the same image with diverse degradation types and varying severity levels. Moreover, each degradation type is parametrized by a set of values that constrain the severity of the distortion. During training, these parameters are randomly selected for each forward pass. Specifically, we utilize 450K images from the Google Landmarks dataset [53] — those with NIMA score higher than 4.90 and with short-edge resolution larger than 400, providing a diverse set of real scenes. Figure 9 show examples for the different degradations under different parameter settings. In what follows, we detail the generation process for each type of synthetic degradation.

Rain: Capturing paired degraded and clean images with rain is inherently challenging, as environmental conditions often vary when capturing the same scene under rainy and clear weather. Consequently, deraining datasets typically simulate rain by creating a set of predefined rain stroke masks, which are then added to input images. However, these datasets often include a limited number of masks [56], leading to potential overfitting on the specific patterns present in the dataset. In our case, aiming to derive a more general set of masks, we consider five adjustable parameters: density, length, angle, drop size, and blending weight.

The process for generating a rainy image I_{rain} begins by creating an empty mask M of the same size as the input image I_{input} , which will hold the rain-stroke patterns. The density parameter d determines the number of raindrops, computed as a fraction of the total image pixels. Random coordinates for the starting positions of the drops are generated, ensuring they stay within bounds to accommodate the specified drop size s . These coordinates are then used to populate M with raindrops. Next, a motion blur kernel K is constructed to simulate the appearance of rain streaks,

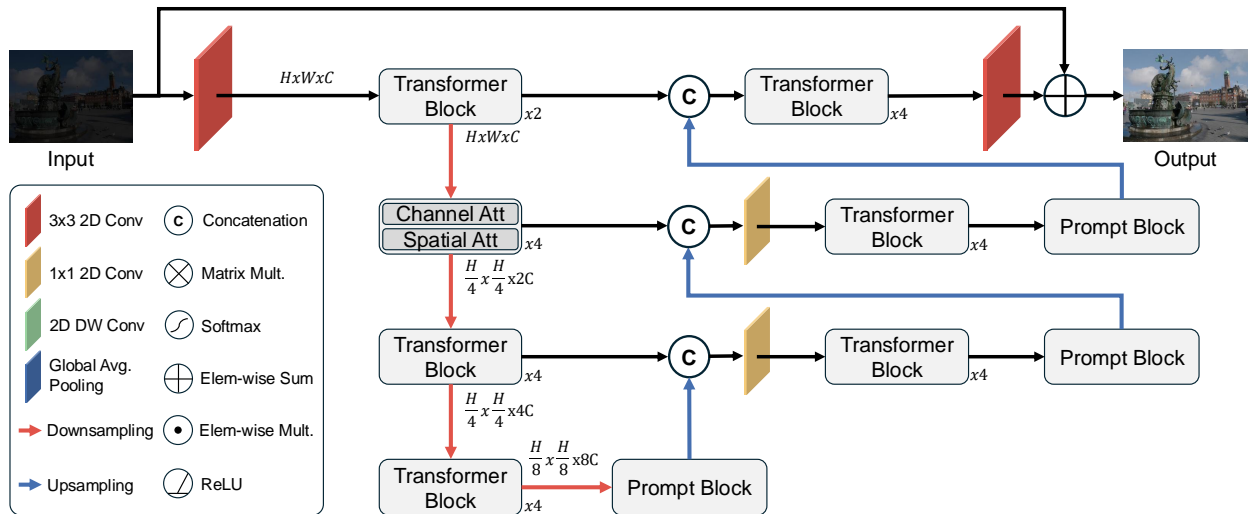


Figure 7. Overview of our baseline model. The input degraded image is processed through a four-level U-shaped network with transformer blocks. In the upsampling path, prompt blocks are integrated to assist the model in capturing degradation-specific information.

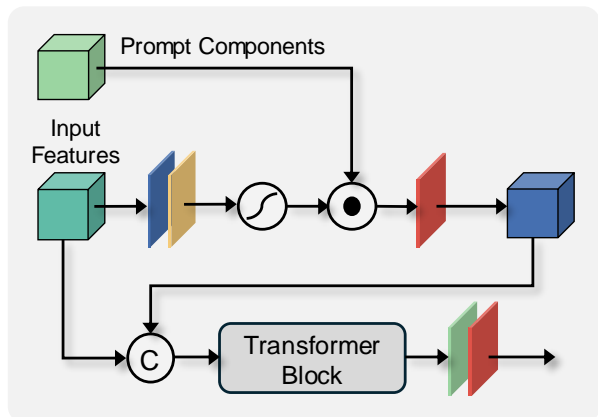


Figure 8. Overview of our Prompt Block. The input features, derived from the output of a transformer block, are modulated through a weighted element-wise multiplication with a set of model parameters. These modulated features are then further refined using an additional transformer block, producing the enhanced output features of the Prompt Block.

based on the specified rain length l and angle θ . The mask M is convolved with K , creating streaks that mimic natural rain patterns. Finally, the rain streaks are normalized and expanded into three RGB channels to match the input image dimensions. These streaks are blended with the original image I_{input} using a weight w , resulting in the final rain-augmented image I_{rain} . All the input parameters are randomly selected for each forward pass. Mathematically—omitting normalizations for clarity,

$$I_{rain} = wI_{input} + (1 - w)(K * M). \quad (2)$$

The value ranges are rain density d : [0.005, 0.02], rain length l : [25, 35], rain angle θ : [70, 110], raindrop size s : [1, 3], and

mask weight [0.75, 1].

Haze: As with rainy images, capturing paired degraded and clean images under hazy conditions is nearly impossible due to the variability of environmental factors. Inspired by prior works [3, 16, 26], we model haze degradation using the Kochsmieder model [17], which describes how the visibility of distant objects diminishes, vanishing into the horizon as a function of their distance from the observer. We can formulate it as:

$$I_{haze} = T \cdot I_{input} + (1 - T) \cdot A, \quad (3)$$

where I_{input} is the input clean image, T is the transmission map derived from the estimated depth map, A is the airlight, and I_{haze} is the resulting image with synthetic haze.

We estimate the depth map of the input image using DepthAnythingv2 [55]. This depth map is normalized within the predefined minimum and maximum haze values to generate the transmission map T . The depth map is then replicated for each color channel to compute Eq. (3). To ensure variability, all parameters are randomly sampled for each forward pass. The parameter ranges are as follows: minimum haze [0.2, 0.4], and maximum haze [0.7, 0.9], airlight is unique for the three color channels with values ranging [140, 200].

Blur: Blur in images can arise from various sources, such as motion blur, out-of-focus blur, and lens blur, among others. In this work, we focus on simulating the motion blur due to its relevance in practical applications. The blur effect is introduced by convolving the input image I_{input} with a parametrized kernel K , designed to model motion blur along a specific direction. The kernel is defined by its size

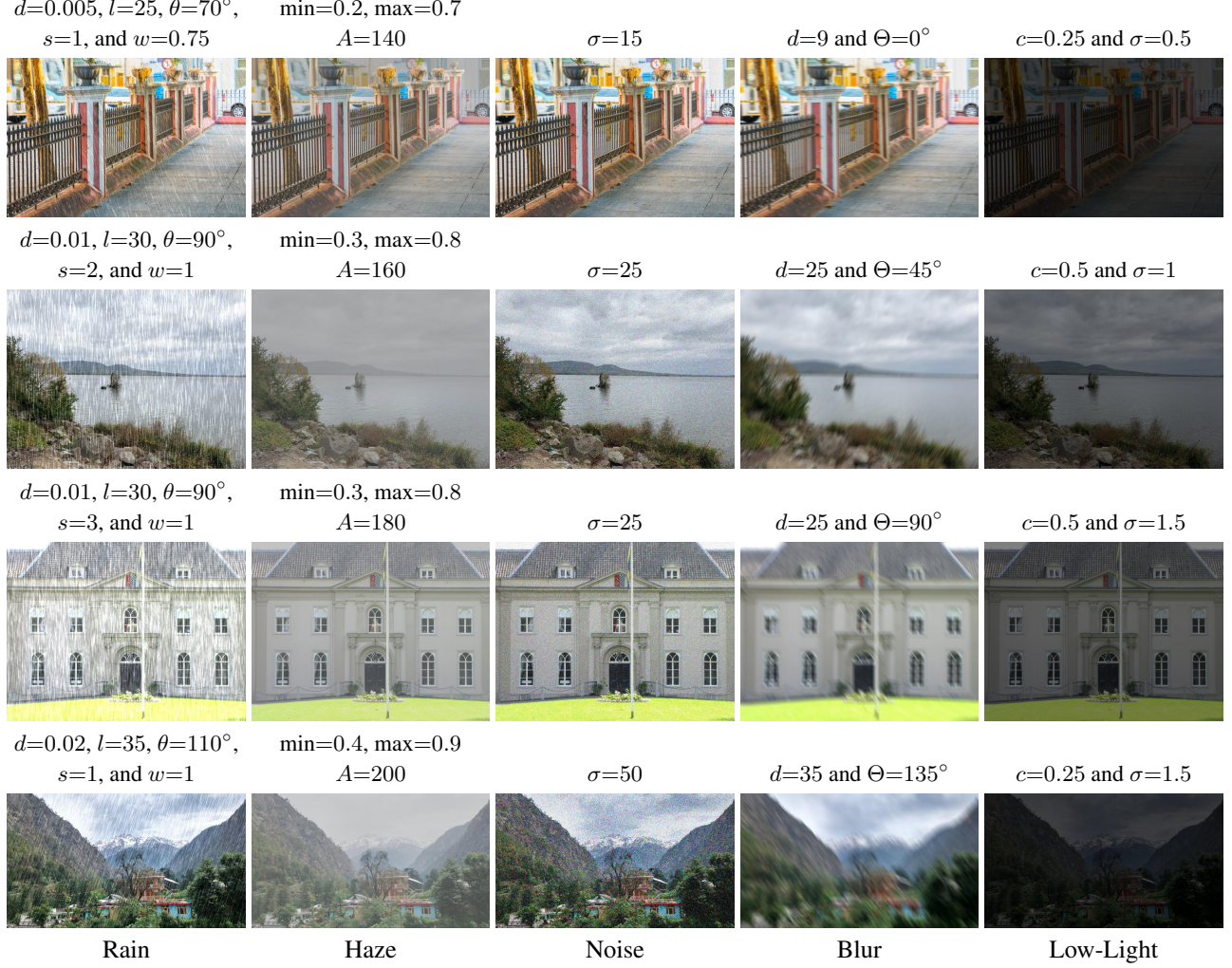


Figure 9. Additional examples showing our synthetic degradation generation for rain, haze, noise, blur, and low-light conditions. On top of each image, we report the specific parameters used to produce the corresponding degraded output.

in pixels (d) and its angle (Θ), to simulate the directional streaks characteristics of motion blur. Mathematically,

$$I_{blur} = K_{\Theta, d} * I_{input}. \quad (4)$$

The kernel size (d) is selected from odd values within the range $[9, 35]$, while the angle (Θ) specifies the orientation of the blur in degrees, ranging from $[0, 360]$.

Noise: We use the standard Additive White Gaussian Noise (AWGN) approach for noise. In short, we add to the original image a second image that follows a Gaussian distribution with mean 0 and variance σ . Mathematically,

$$I_{noise} = I_{input} + \mathcal{N}(0, \sigma). \quad (5)$$

Low-Light: When an image is captured under low-light conditions, cameras amplify the sensor’s signal to capture

details, amplifying noise, and leading to grainy or speckled artifacts. Furthermore, the reduced dynamic range limits the ability to capture the range of intensities, resulting in color inconsistencies, and loss of detail in shadows and highlights. To simulate these conditions, we compress the input image histogram by a factor c and add a noise with a meager σ value. This process can be expressed mathematically as:

$$I_{lol} = I_{input} \cdot c + \mathcal{N}(0, \sigma). \quad (6)$$

The compression factor c ranges in the interval $[0.25, 0.5]$ and the σ takes values in the interval $[0.5, 1.5]$.

C. Additional Phase II Ablation Studies

The second phase of our approach involves training a set of adapters — LoRA [19] in the main manuscript — for each type of degradation. In this section, we extend our analysis

Table 7. Ablation study on different low-rank adapters and their rank. Results are the mean for all images. LoRA outperforms both VeRA and Conv-LORA. Lower ranks perform better.

PSNR/SSIM		Deraining		Dehazing		Denoising		Deblurring		Low-Light		Average		Adapter Param.
Method	Rank	Rain100L		SOTS (Out)		BSD68 $\sigma=25$		GoPro		LoLv1				
LoRA [19]	4	37.79	.979	33.48	.984	31.38	.898	29.00	.878	24.19	.865	31.17	.921	3.6M
	8	37.75	.978	33.4	.982	31.39	.898	29.02	.878	24.18	.865	31.15	.920	7.2M
	16	37.61	.972	33.21	.977	31.31	.896	28.77	.875	23.96	.862	30.97	.916	14.3M
VeRA [24]	4	37.02	.971	32.67	.972	31.32	.896	28.61	.872	23.78	.580	30.68	.858	460K
	8	37.09	.971	32.69	.972	31.32	.896	28.64	.873	23.79	.580	30.71	.858	468K
	16	37.04	.970	32.62	.970	31.33	.896	28.62	.872	23.84	.581	30.69	.858	476K
Conv-LoRA [67]	4	37.00	.969	32.55	.971	31.32	.896	28.54	.870	23.70	.576	30.62	.856	3.9M
	8	36.94	.968	32.44	.968	31.30	.895	28.48	.868	23.62	.575	30.56	.855	7.5M

to include other low-rank decompositions and their rank. Specifically, we evaluate VeRA [24] and Conv-LoRA [67]. The results for the five-degradation setup across the three adapter types are presented in Tab. 7, which also includes the number of trainable parameters for each adapter in the last column. For a fair comparison, we utilize the same baseline model weights and estimator, while training only the task-specific adapters. Among the methods, LoRA [19] achieves the best overall performance. However, VeRA [24] provides competitive results with significantly fewer parameters, as it estimates only two vectors per layer instead of two low-rank matrices. On the other hand, Conv-LoRA [67] performs worse despite having more parameters, owing to its Mixture-of-Experts approach with convolution layers in the decomposed space. Regarding the decomposition rank, we find that ranks of 4 and 8 consistently outperform a rank of 16 in terms of both accuracy and parameter efficiency.

D. Additional Phase III Analysis

In the third phase of our method, we train an estimator to select or blend the most suitable set of adapters based on the input image. The estimator architecture comprises four blocks of Conv2D layers, each followed by batch normalization, ReLU activation, and max pooling, culminating with a global average pooling layer and a linear projection. The total parameter count for the estimator is 538K.

We present a confusion matrix in Fig. 10, showing the One-Hot predictions for known degradations —both seen and unseen datasets. The estimator predicts known degradations with probabilities exceeding 90% in most cases. However, for one of the unseen datasets, the Rain100H dataset [56], the prediction probability falls below 90%, likely due to the severity of the rain streaks and their resemblance to haze-related degradations. Notably, even when the estimator selects an incorrect adapter, no significant artifacts or undesired effects are introduced, owing to the robustness of the large-scale pre-training.

Finally, to highlight the importance of our estimator,

we perform a last ablation comparing our approach to just adding or averaging the five degradation task-specific adapters. Tab. 8 shows the results of this ablation. When all adapters are added, the ΔW values become excessively large for the baseline model to effectively handle them. On the other hand, averaging the adapters results in suboptimal restored images, as the model fails to specialize in any particular degradation type.

E. Additional Qualitative Results

Figure 11 presents additional qualitative results for known degradations, including examples from both seen and unseen datasets. Figure 12 highlights results for unknown degradations, with the corresponding mean absolute error (MAE) map displayed below each image to emphasize the differences. Finally, Figure 13 shows qualitative results for mixed degradation scenarios.

Table 8. Ablation study on different methods for blending the five degradations task-specific LoRA [19] adapters.

PSNR/SSIM Method	Deraining		Dehazing		Denoising		Deblurring		Low-Light		Average	
	Rain100L		SOTS (Out)		BSD68 $\sigma=25$		GoPro		LoLv1			
Sum	19.50	.755	18.80	.745	18.10	.730	18.25	.728	17.70	.715	18.67	.736
Average	30.54	.939	20.87	.855	28.98	.785	21.34	.792	15.49	.673	23.84	.809
Ours OH	37.73	.978	33.46	.983	31.38	.898	29.00	.878	24.20	.865	31.15	.920
Ours SW	37.79	.979	33.48	.984	31.38	.898	29.00	.878	24.19	.865	31.17	.921



Figure 10. Confusion matrix for our estimator in test images. First five columns: known degradations with the datasets considered at training. Last three columns: unknown datasets for rain, blur, and low light. Specifically, from left-to-right columns, the datasets are: Rain100L [56], BSD68 [33], SOTS (outdoors) [26], GoPro [35], LoLv1 [52], Rain100H [56], HIDE [43], and LoLv2-Real [57].

References

- [1] Samira Abnar, Mostafa Dehghani, Behnam Neyshabur, and Hanie Sedghi. Exploring the limits of large scale pre-training. In *ICLR*, 2022. 4
- [2] Yuang Ai, Huaibo Huang, Xiaoqiang Zhou, Jiexiang Wang, and Ran He. Multimodal prompt perceiver: Empower adaptiveness generalizability and fidelity for all-in-one image restoration. In *CVPR*, 2024. 2
- [3] Cosmin Ancuti, Codruta O. Ancuti, and Christophe De Vleeschouwer. D-hazy: A dataset to evaluate quantitatively dehazing algorithms. In *ICIP*, pages 2226–2230, 2016. 10
- [4] Yuanhao Cai, Hao Bian, Jing Lin, Haoqian Wang, Radu Timofte, and Yulun Zhang. Retinexformer: One-stage retinex-based transformer for low-light image enhancement. In *ICCV*, 2023. 1, 2
- [5] Liangyu Chen, Xiaojie Chu, Xiangyu Zhang, and Jian Sun. Simple baselines for image restoration. In *ECCV*, 2022. 2
- [6] Wei-Ting Chen, Hao-Yu Fang, Jian-Jiun Ding, Cheng-Che Tsai, and Sy-Yen Kuo. Jstsr: Joint size and transparency-aware snow removal algorithm based on modified partial convolution and veiling effect removal. In *ECCV*, pages 754–770. Springer, 2020. 7, 8, 15
- [7] Xiang Chen, Hao Li, Mingqiang Li, and Jinshan Pan. Learning a sparse transformer network for effective image deraining. In *CVPR*, pages 5896–5905, 2023. 2
- [8] Xiangyu Chen, Zheyuan Li, Yuandong Pu, Yihao Liu, Jiantao Zhou, Yu Qiao, and Chao Dong. A comparative study of image restoration networks for general backbone network design. *arXiv preprint arXiv:2310.11881*, 2023. 2, 4, 5, 6, 8, 9
- [9] Xiangyu Chen, Xintao Wang, Jiantao Zhou, Yu Qiao, and Chao Dong. Activating more pixels in image super-resolution transformer. In *CVPR*, pages 22367–22377, 2023. 9
- [10] Matthias De Lange, Rahaf Aljundi, Marc Masana, Sarah Parisot, Xu Jia, Aleš Leonardis, Gregory Slabaugh, and Tinne Tuytelaars. A continual learning survey: Defying forgetting in classification tasks. *IEEE TPAMI*, 44(7):3366–3385, 2022. 3
- [11] Mauricio Delbracio and Peyman Milanfar. Inversion by di-

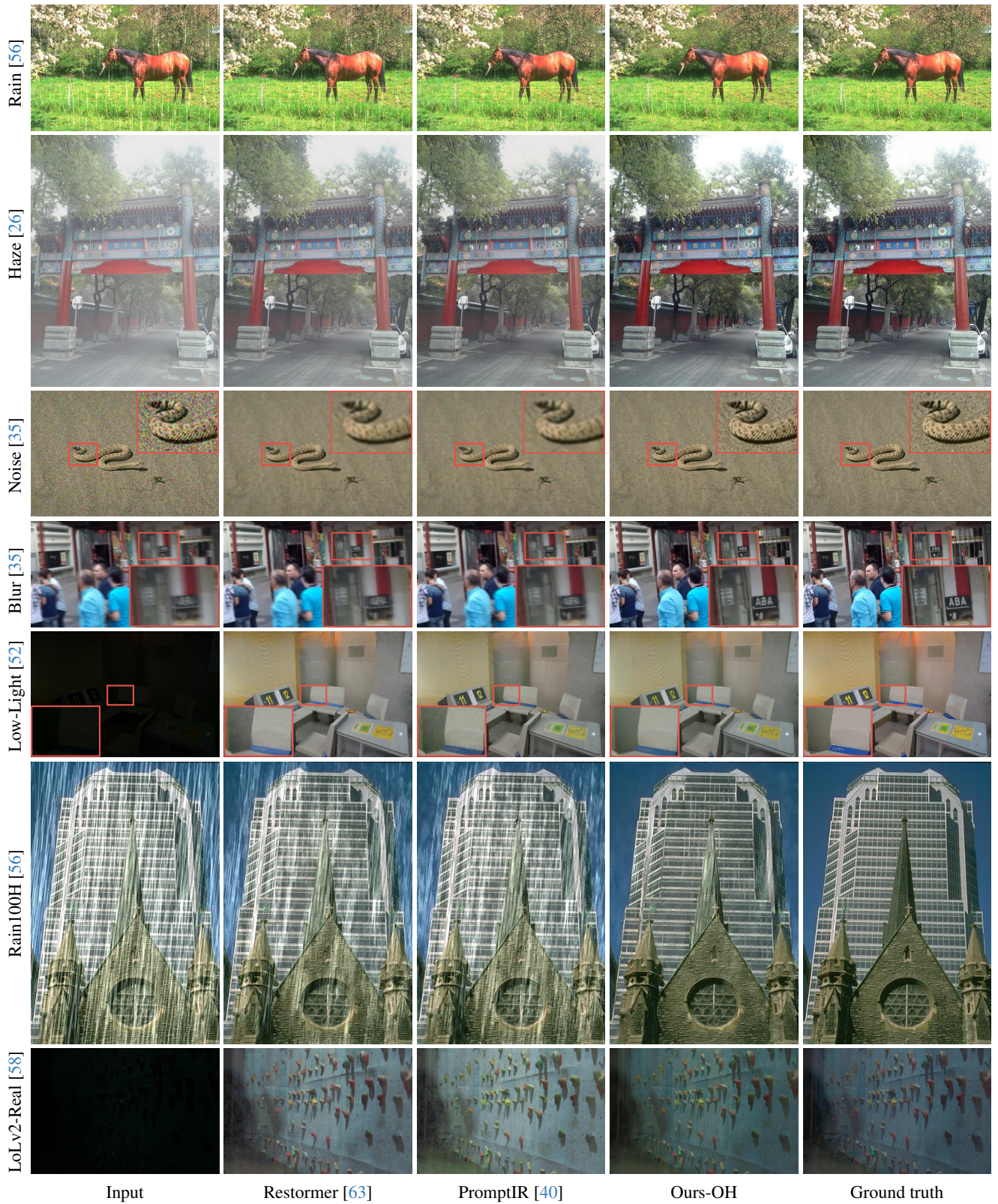


Figure 11. Qualitative results for known degradation removal, both seen datasets —Rows 1 to 5— and unseen datasets —Rows 6 to 8.

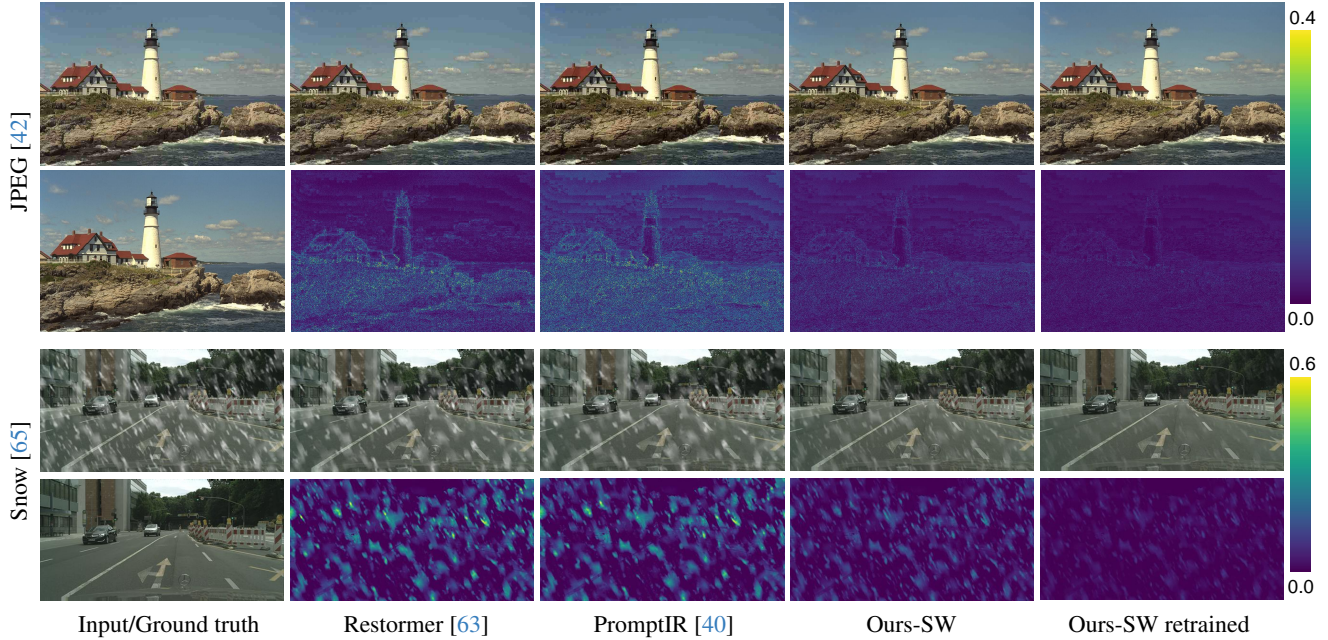


Figure 12. Qualitative results on JPEG artifact removal on Live1 dataset [42] and desnowing on CityScapes-Snow-Medium [65]. We show the mean absolute error map below each image.



Figure 13. Qualitative results on mixed degradation scenarios. Specifically, blur and JPEG on the REDS [36] dataset and haze and snow in the SRRS [6] dataset.

- rect iteration: An alternative to denoising diffusion for image restoration. *TMLR*, 2023. 1
- [12] Weisheng Dong, Lei Zhang, Guangming Shi, and Xiaolin Wu. Image deblurring and super-resolution by adaptive sparse domain selection and adaptive regularization. *IEEE TIP*, 20(7):1838–1857, 2011. 1
- [13] Weisheng Dong, Peiyao Wang, Wotao Yin, Guangming Shi, Fangfang Wu, and Xiaotong Lu. Denoising prior driven deep neural network for image restoration. *IEEE TPAMI*, 41(10):2305–2318, 2018. 1, 2
- [14] Qingnan Fan, Dongdong Chen, Lu Yuan, Gang Hua, Nenghai Yu, and Baoquan Chen. A general decoupled learning framework for parameterized image operators. *IEEE TPAMI*, 43(1):33–47, 2019. 6
- [15] Sina Farsiu, M Dirk Robinson, Michael Elad, and Peyman Milanfar. Fast and robust multiframe super resolution. *IEEE TIP*, 13(10):1327–1344, 2004. 1
- [16] Adrian Galdran, Javier Vazquez-Corral, David Pardo, and Marcelo Bertalmío. Enhanced variational image dehazing. *SIAM Journal on Imaging Sciences*, 8(3):1519–1546, 2015. 10
- [17] Koschmieder Harald. Theorie der horizontalen sichtweite: Kontrast und sichtweite. *Keim and Nennich, Munich*, 12, 1924. 10
- [18] Kaiming He, Jian Sun, and Xiaoou Tang. Single image haze removal using dark channel prior. *IEEE TPAMI*, 33(12):2341–2353, 2010. 1
- [19] Edward J Hu, Yelong Shen, Phillip Wallis, Zeyuan Allen-

- Zhu, Yuanzhi Li, Shean Wang, Lu Wang, and Weizhu Chen. Lora: Low-rank adaptation of large language models. In *ICLR*, 2021. 2, 3, 8, 11, 12, 13
- [20] Menglin Jia, Luming Tang, Bor-Chun Chen, Claire Cardie, Serge Belongie, Bharath Hariharan, and Ser-Nam Lim. Visual prompt tuning. In *ECCV*, 2022. 2
- [21] Kwang In Kim and Younghee Kwon. Single-image super-resolution using sparse regression and natural image prior. *IEEE TPAMI*, 32(6):1127–1133, 2010. 1
- [22] Stefan Kindermann, Stanley Osher, and Peter W Jones. Deblurring and denoising of images by nonlocal functionals. *Multiscale Modeling & Simulation*, 4(4):1091–1115, 2005. 1
- [23] Diederik P Kingma and Jimmy Ba. Adam: A method for stochastic optimization. In *ICLR*, 2015. 5
- [24] Dawid Jan Kopiczko, Tijmen Blankevoort, and Yuki M Asano. VeRA: Vector-based random matrix adaptation. In *ICLR*, 2024. 3, 12
- [25] Boyi Li, Wenqi Ren, Dengpan Fu, Dacheng Tao, Dan Feng, Wenjun Zeng, and Zhangyang Wang. Benchmarking single-image dehazing and beyond. *IEEE TIP*, 28(1):492–505, 2018. 6
- [26] Boyi Li, Wenqi Ren, Dengpan Fu, Dacheng Tao, Dan Feng, Wenjun Zeng, and Zhangyang Wang. Benchmarking single-image dehazing and beyond. *IEEE TIP*, 28(1):492–505, 2019. 10, 13, 14
- [27] Boyun Li, Xiao Liu, Peng Hu, Zhongqin Wu, Jiancheng Lv, and Xi Peng. All-in-one image restoration for unknown corruption. In *CVPR*, 2022. 1, 2, 5, 6
- [28] Ruoteng Li, Robby T. Tan, and Loong-Fah Cheong. All in one bad weather removal using architectural search. In *CVPR*, 2020. 1
- [29] I Loshchilov. Decoupled weight decay regularization. In *ICLR*, 2019. 5
- [30] Ziwei Luo, Fredrik K Gustafsson, Zheng Zhao, Jens Sjölund, and Thomas B Schön. Controlling vision-language models for universal image restoration. *arXiv preprint arXiv:2310.01018*, 3(8), 2023. 2, 5
- [31] Jiaqi Ma, Tianheng Cheng, Guoli Wang, Qian Zhang, Xinggang Wang, and Lefei Zhang. Prores: Exploring degradation-aware visual prompt for universal image restoration. *arXiv preprint arXiv:2306.13653*, 2023. 2
- [32] Kede Ma, Zhengfang Duanmu, Qingbo Wu, Zhou Wang, Hongwei Yong, Hongliang Li, and Lei Zhang. Waterloo exploration database: New challenges for image quality assessment models. *IEEE TIP*, 26(2):1004–1016, 2016. 6
- [33] David Martin, Charless Fowlkes, Doron Tal, and Jitendra Malik. A database of human segmented natural images and its application to evaluating segmentation algorithms and measuring ecological statistics. In *ICCV*, 2001. 6, 13
- [34] Tomer Michaeli and Michal Irani. Nonparametric blind super-resolution. In *ICCV*, 2013. 1
- [35] Seungjun Nah, Tae Hyun Kim, and Kyoung Mu Lee. Deep multi-scale convolutional neural network for dynamic scene deblurring. In *CVPR*, 2017. 6, 7, 8, 13, 14
- [36] Seungjun Nah, Sungyong Baik, Seokil Hong, Gyeongsik Moon, Sanghyun Son, Radu Timofte, and Kyoung Mu Lee. Ntire 2019 challenge on video deblurring and super-resolution: Dataset and study. In *CVPR Workshops*, pages 0–0, 2019. 7, 15
- [37] Xuejing Niu, Bo Yan, Weimin Tan, and Junyi Wang. Effective image restoration for semantic segmentation. *Neurocomputing*, 374:100–108, 2020. 1
- [38] Joao P Oliveira, José M Bioucas-Dias, and Mário AT Figueiredo. Adaptive total variation image deblurring: a majorization–minimization approach. *Signal processing*, 89(9):1683–1693, 2009. 1
- [39] Dongwon Park, Hayeon Kim, and Se Young Chun. Contribution-based low-rank adaptation with pre-training model for real image restoration. In *ECCV*, 2024. 2, 3
- [40] Vaishnav Potlapalli, Syed Waqas Zamir, Salman H Khan, and Fahad Shahbaz Khan. Promptir: Prompting for all-in-one image restoration. In *NeurIPS*, 2024. 1, 2, 4, 5, 6, 7, 8, 9, 14, 15
- [41] Mengwei Ren, Mauricio Delbracio, Hossein Talebi, Guido Gerig, and Peyman Milanfar. Multiscale structure guided diffusion for image deblurring. In *ICCV*, 2023. 1, 2
- [42] Hamid R Sheikh, Muhammad F Sabir, and Alan C Bovik. A statistical evaluation of recent full reference image quality assessment algorithms. *IEEE TIP*, 15(11):3440–3451, 2006. 7, 8, 15
- [43] Ziyi Shen, Wenguan Wang, Xiankai Lu, Jianbing Shen, Haibin Ling, Tingfa Xu, and Ling Shao. Human-aware motion deblurring. In *ICCV*, pages 5572–5581, 2019. 6, 13
- [44] Wenzhe Shi, Jose Caballero, Ferenc Huszár, Johannes Totz, Andrew P Aitken, Rob Bishop, Daniel Rueckert, and Zehan Wang. Real-time single image and video super-resolution using an efficient sub-pixel convolutional neural network. In *CVPR*, pages 1874–1883, 2016. 9
- [45] Shangquan Sun, Wenqi Ren, Tao Wang, and Xiaochun Cao. Rethinking image restoration for object detection. In *NeurIPS*, 2022. 1
- [46] Hossein Talebi and Peyman Milanfar. Nima: Neural image assessment. *IEEE TIP*, 27(8):3998–4011, 2018. 4
- [47] Radu Timofte, Vincent De Smet, and Luc Van Gool. Anchored neighborhood regression for fast example-based super-resolution. In *ICCV*, 2013. 1
- [48] Jeya Maria Jose Valanarasu, Rajeev Yasarla, and Vishal M Patel. Transweather: Transformer-based restoration of images degraded by adverse weather conditions. In *CVPR*, 2022. 1
- [49] Cong Wang, Jinshan Pan, Wanyu Lin, Jiangxin Dong, Wei Wang, and Xiao-Ming Wu. Selfpromer: Self-prompt dehazing transformers with depth-consistency. In *AAAI*, 2024. 1
- [50] Xinlong Wang, Wen Wang, Yue Cao, Chunhua Shen, and Tiejun Huang. Images speak in images: A generalist painter for in-context visual learning. In *CVPR*, 2023. 2
- [51] Zhendong Wang, Xiaodong Cun, Jianmin Bao, Wengang Zhou, Jianzhuang Liu, and Houqiang Li. Uformer: A general u-shaped transformer for image restoration. In *CVPR*, pages 17683–17693, 2022. 5
- [52] Chen Wei, Wenjing Wang, Wenhan Yang, and Jiaying Liu. Deep retinex decomposition for low-light enhancement. In *BMVC*, 2018. 6, 7, 13, 14

- [53] Tobias Weyand, Andre Araujo, Bingyi Cao, and Jack Sim. Google landmarks dataset v2-a large-scale benchmark for instance-level recognition and retrieval. In *CVPR*, pages 2575–2584, 2020. 4, 9
- [54] Lingling Xu, Haoran Xie, Si-Zhao Joe Qin, Xiaohui Tao, and Fu Lee Wang. Parameter-efficient fine-tuning methods for pretrained language models: A critical review and assessment. *arXiv preprint arXiv:2312.12148*, 2023. 3
- [55] Lihe Yang, Bingyi Kang, Zilong Huang, Zhen Zhao, Xiaogang Xu, Jiashi Feng, and Hengshuang Zhao. Depth anything v2. *arXiv preprint arXiv:2406.09414*, 2024. 4, 10
- [56] Wenhan Yang, Robby T Tan, Jiashi Feng, Jiaying Liu, Zongming Guo, and Shuicheng Yan. Deep joint rain detection and removal from a single image. In *CVPR*, pages 1357–1366, 2017. 6, 7, 9, 12, 13, 14
- [57] Wenhan Yang, Shiqi Wang, Yuming Fang, Yue Wang, and Jiaying Liu. From fidelity to perceptual quality: A semi-supervised approach for low-light image enhancement. In *CVPR*, 2020. 13
- [58] Wenhan Yang, Wenjing Wang, Haofeng Huang, Shiqi Wang, and Jiaying Liu. Sparse gradient regularized deep retinex network for robust low-light image enhancement. *IEEE TIP*, 30:2072–2086, 2021. 6, 14
- [59] Yang Yang, Chaoyue Wang, Risheng Liu, Lin Zhang, Xiaojie Guo, and Dacheng Tao. Self-augmented unpaired image dehazing via density and depth decomposition. In *CVPR*, 2022. 2
- [60] Zongsheng Yue, Jianyi Wang, and Chen Change Loy. Efficient diffusion model for image restoration by residual shifting. In *NeurIPS*, 2024. 2
- [61] Sangdoon Yun, Dongyoon Han, Seong Joon Oh, Sanghyuk Chun, Junsuk Choe, and Youngjoon Yoo. Cutmix: Regularization strategy to train strong classifiers with localizable features. In *ICCV*, 2019. 2, 4, 8
- [62] Syed Waqas Zamir, Aditya Arora, Salman Khan, Munawar Hayat, Fahad Shahbaz Khan, Ming-Hsuan Yang, and Ling Shao. Multi-stage progressive image restoration. In *CVPR*, 2021. 2, 6
- [63] Syed Waqas Zamir, Aditya Arora, Salman Khan, Munawar Hayat, Fahad Shahbaz Khan, and Ming-Hsuan Yang. Restormer: Efficient transformer for high-resolution image restoration. In *CVPR*, 2022. 1, 2, 4, 5, 6, 7, 8, 9, 14, 15
- [64] Jinghao Zhang, Jie Huang, Mingde Yao, Zizheng Yang, Hu Yu, Man Zhou, and Feng Zhao. Ingredient-oriented multi-degradation learning for image restoration. In *CVPR*, 2023. 2, 5, 6, 8
- [65] Kaihao Zhang, Rongqing Li, Yanjiang Yu, Wenhan Luo, and Changsheng Li. Deep dense multi-scale network for snow removal using semantic and geometric priors. *IEEE TIP*, 2021. 7, 15
- [66] Dian Zheng, Xiao-Ming Wu, Shuzhou Yang, Jian Zhang, Jian-Fang Hu, and Wei-Shi Zheng. Selective hourglass mapping for universal image restoration based on diffusion model. In *CVPR*, 2024. 1, 2, 5, 6, 8
- [67] Zihan Zhong, Zhiqiang Tang, Tong He, Haoyang Fang, and Chun Yuan. Convolution meets loRA: Parameter efficient finetuning for segment anything model. In *ICLR*, 2024. 3, 12
- [68] Dewei Zhou, Zongxin Yang, and Yi Yang. Pyramid diffusion models for low-light image enhancement. In *IJCAI*, 2024. 1, 2